
POTENTIAL FOR DAMAGE TO FRUITS DURING TRANSPORT THROUGH CROSS-SECTION CONSTRICTIONS

A PREPRINT

 **Jan E. Marquardt***

Lattice Boltzmann Research Group
Institute of Mechanical Process Engineering and Mechanics
Karlsruhe Institute of Technology
76131 Karlsruhe, Germany
jan.marquardt@kit.edu

 **Bastian Eysel**

Institute of Food Biotechnology and Food Process Engineering
Faculty III Process Sciences
Technische Universität Berlin
10623 Berlin, Germany

 **Martin Sadric**

Lattice Boltzmann Research Group
Institute for Applied and Numerical Mathematics
Karlsruhe Institute of Technology
76131 Karlsruhe, Germany

 **Cornelia Rauh**

Institute of Food Biotechnology and Food Process Engineering
Faculty III Process Sciences
Technische Universität Berlin
10623 Berlin, Germany

 **Mathias J. Krause**

Lattice Boltzmann Research Group
Institute for Applied and Numerical Mathematics
Karlsruhe Institute of Technology
76131 Karlsruhe, Germany

September 2, 2024

ABSTRACT

Fruit preparations are used in various forms in the food industry. For example, they are used as an ingredient in dairy products such as yogurt with added fruit. The dispersed fruit pieces can be described as soft particles with viscoelastic material behavior. The continuous phase is represented by fluids with complex flow behavior depending on the formulation. Characterization has shown that this can be described by the Herschel–Bulkley model. Since damage to fruit pieces is undesirable in industrial transport processes, the potential for damage to fruit pieces during transport of pipes in cross-sectional constrictions is analyzed. The analysis is performed numerically using the homogenized

*Corresponding author

lattice Boltzmann method and validated by an experiment on industrial fruit preparations at pilot plant scale. The results show a strong dependence of the damage potential on the (local) Metzner–Reed Reynolds number.

Keywords particulate flow · particle-resolved simulation · homogenized lattice Boltzmann method.

1 Introduction

Many food products can be described as suspensions of mechanically sensitive, i.e. deformable or fragile, particles. Examples include chunky fruit preparations commonly used in the dairy industry, such as fruit yogurt. During the manufacturing process, transport through piping and various fittings (e.g. pipe constrictions/expansions, valves, pumps, flaps, bends) plays a significant role and leads to a high potential for damage. During this transport, the particle component is subjected to mechanical stresses due to hydrodynamic forces and collisions with other particles or with apparatus parts. These stresses are highly variable in intensity and transient in nature.

Literature primarily focuses on pipeline transport of coarse-dispersed food suspensions to avoid under-processing during thermal treatment [1, 2]. Flow conditions are characterized based on the solid volume fraction and other dimensionless parameters (Reynolds number, particle Reynolds number, particle Froude number, Stokes number) [3], facilitating the identification of various regimes describing the distribution of the particle component across the pipe [4, 5]. Such concentrated suspensions must flow at relatively high velocities to maintain a homogeneous particle distribution. Heterogeneous flow occurs when a gradient in particle concentration is evident, with cases of pronounced gradients distinguished as moving bed and stationary bed formations [6].

Laminar flows of suspensions of (usually spherical) particles of similar density to the surrounding fluid have been studied experimentally [1, 2, 7–9] and numerically [10–14]. However, the focus of these works is on the particle-fluid interaction, not the potential damage.

Thus, while the behavior of laminar, particle-laden flows in pipelines is partially understood, this is not the case for mechanical damage to the particulate phase. Considerations of damage have been limited to harvesting, packaging, and vehicle transport of fresh fruits [15]. In the context of food processing, only the influence of pumps on particle damage has been studied using the example of rotary lobe and centrifugal pumps [16]. However, unlike pumps, the stress in piping systems can be expected to be cyclical and increasing/decreasing as particles move continuously with the flow. Individual events are not necessarily binary. Rather, fruit preparations are subjected to several successive transport processes, so that the entire history plays a role. The resulting strain is quantified on the basis of collision, shear and elongation effects [17, 18]. Their importance for the momentum and energy coupling between disperse and continuous phase depends strongly on the characteristic length scales and the material consistency of the coarsely dispersed phase. In the case of (approximately) deformation-resistant fruit pieces, the coupling is largely achieved by viscous forces at the surface and normal forces caused by the pressure distribution.

Despite the existing research on laminar particle-laden flows and particle-fluid interactions, there is a significant gap in the understanding of mechanical damage to the particle component, particularly in the context of the transport of food suspensions through piping systems. The unique stress conditions in such systems have not been investigated, highlighting the need for a comprehensive study to address these knowledge gaps, with a particular focus on the impact of pipeline transport on the quality and integrity of food suspensions.

Therefore, the aim of this research paper is to investigate the damage potential of the particulate component of food suspensions during their flow through piping systems, in particular cross-sectional constrictions, under practical and relevant conditions, including process parameters and material properties. The objective of the work is to investigate and understand the mutual influence between the continuous and dispersed phases, to identify and analyze the types and intensities of stresses that occur during flow, and to determine which of these stresses are primarily responsible for significant particle damage. In addition, the spatial dependencies of the flow-induced stresses caused by the geometries of the equipment are investigated, and the main parameters influencing the damage of the particle phase are determined, while the interactions between them are studied. To achieve these objectives, the current work uses a combination of experiments and simulations, providing a comprehensive and in-depth analysis of the mechanical stresses and damage experienced by food particles during transport through pipes with cross-sectional constrictions. Ultimately, the knowledge gained supports the design of piping systems in food processing to improve the quality and integrity of food products.

To this end, the following sections are organized as follows. Section 2 presents the models that describe the fluid and the particle, while Section 3 discusses the numerical methods used for the simulations. In Section 4 we outline the experimental and computational setups and in Section 5 we present the results of the following studies. Finally, the key findings and conclusions of this study are summarized in Section 6.

2 Modeling

2.1 Fluid

Fluids are generally considered to be incompressible. In this case, the Navier–Stokes equations become

$$\begin{aligned} \frac{\partial \mathbf{u}_f}{\partial t} + (\mathbf{u}_f \cdot \nabla) \mathbf{u}_f - \nu \Delta \mathbf{u}_f + \frac{1}{\rho_f} \nabla p &= \frac{\mathbf{F}_f}{\rho_f}, \\ \nabla \cdot \mathbf{u}_f &= 0, \end{aligned} \quad (1)$$

where p is the pressure, t is the time, \mathbf{F}_f is the total of all forces acting on the fluid and \mathbf{u}_f , ρ_f , η are the velocity, density and dynamic viscosity of the fluid.

For Newtonian fluids, η is a constant. For non-Newtonian fluids, however, the viscosity depends on the shear rate $\dot{\gamma}$. Power laws are usually used to represent this dependency. Using the Herschel–Bulkley relation, the effective viscosity is given by [19]

$$\eta^* = \tau_0 |\dot{\gamma}|^{-1} + k |\dot{\gamma}|^{n-1}, \quad (2)$$

with the yield stress τ_0 , consistency index k , and power law index n . Since this equation diverges for $\dot{\gamma} \rightarrow 0$, a minimal shear rate $\dot{\gamma}_{\min}$ is usually used in the equation above for $\dot{\gamma} < \dot{\gamma}_{\min}$.

When the regarded fluid has a yield stress $\tau_0 = 0$, then the above simplifies to the Ostwald–de Waele relation, for which the effective viscosity reads [20]

$$\eta^* = k |\dot{\gamma}|^{n-1}. \quad (3)$$

2.2 Particle

For the particle component, we use Newton’s second law of motion. Therefore, translation is described by

$$m_p \frac{\partial \mathbf{u}_p}{\partial t} = \mathbf{F}_p \quad (4)$$

and rotation by

$$\mathbf{I}_p \frac{\partial \boldsymbol{\omega}_p}{\partial t} + \boldsymbol{\omega}_p \times (\mathbf{I}_p \cdot \boldsymbol{\omega}_p) = \mathbf{T}_p. \quad (5)$$

Here, m_p , \mathbf{I}_p , \mathbf{u}_p , $\boldsymbol{\omega}_p$ are the mass, moment of inertia, velocity, and angular velocity of the particle, respectively. \mathbf{F}_p and \mathbf{T}_p are the sum of the acting forces and torque affecting the particle motion, respectively. Above, the subscript p indicates that the quantities refer to the particle’s center of mass.

2.3 Contact

In order to accurately model interactions involving complex particle geometries, we employ a contact model that allows for arbitrarily shaped bodies [21]. The normal contact force in this model is given by

$$\mathbf{F}_{c,n} = \frac{4}{3\pi} \mathbf{n}_c E^* \sqrt{V_c \delta} (1 + c \dot{\delta}_n). \quad (6)$$

In this equation, E^* is the effective Young’s modulus, V_c is the overlap volume, δ is the indentation depth, c is a damping factor, and $\dot{\delta}_n$ is the relative velocity between two particles in contact along the contact normal \mathbf{n}_c . The effective Young’s modulus is

$$E^* = \left(\frac{1 - \nu_A^2}{E_A} + \frac{1 - \nu_B^2}{E_B} \right)^{-1}, \quad (7)$$

where E_A and ν_A are the Young’s modulus and Poisson’s ratio of particle A, and E_B and ν_B are those of another solid object B. The damping factor c is related to the coefficient of restitution e as follows [22]

$$c = \begin{cases} 1.5 \frac{(1-e)(11-e)}{(1+9e)u_0} & \text{for } u_0 > 0 \\ 0 & \text{for } u_0 \leq 0 \end{cases}, \quad (8)$$

where u_0 is the relative velocity at the initial contact. Tangential forces, which are influenced by normal forces and the coefficients of static and kinetic friction (μ_s and μ_k), are described by

$$\mathbf{F}_{c,t} = - \frac{\mathbf{u}_{AB,t}(\mathbf{x}_c)}{\|\mathbf{u}_{AB,t}(\mathbf{x}_c)\|} \left((2\mu_s^* - \mu_k) \frac{a^2}{a^4 + 1} + \mu_k - \frac{\mu_k}{a^2 + 1} \right) \|\mathbf{F}_{c,n}\|, \quad (9)$$

with

$$\mu_s^* = \mu_s \left(1 - 0.09 \left(\frac{\mu_k}{\mu_s} \right)^4 \right), \quad (10)$$

and

$$a = \frac{\|\mathbf{u}_{AB,t}(\mathbf{x}_c)\|}{u_k}. \quad (11)$$

Here, $\mathbf{u}_{AB,t}$ is the relative tangential between the two solids A and B, and u_k is the velocity at which the transition from static to kinetic friction occurs, which we set to 0.01 m s^{-1} .

3 Numerical Methods

In the following, the numerical methods used for the simulations are introduced. Note that the all values in Section 3 are given in lattice units, unless explicitly stated otherwise.

All methods presented below are implemented in the open source software OpenLB [23, 24], which is used in this work.

3.1 Lattice Boltzmann method

We use the lattice Boltzmann method (LBM) [25–27] to solve the Navier–Stokes equations for incompressible flows.

LBM has its roots in gas kinetics, which explains why it operates at the mesoscopic level and considers the behavior of fluid particle populations. The discrete velocity distribution function $f_i(\mathbf{x}, t)$ is used to characterize these populations at a position \mathbf{x} and time t . The index i refers to the corresponding discrete velocity \mathbf{c}_i , which is given by the selected velocity set. There are several velocity sets available in literature [25, 26]. We choose the D3Q19, which discretizes the three-dimensional space and contains of 19 discrete velocities, for the studies in this paper. The populations are also used to derive macroscopic quantities such as density $\rho_f(\mathbf{x}, t) = \sum_i f_i(\mathbf{x}, t)$ and velocity $\rho_f \mathbf{u}_f(\mathbf{x}, t) = \sum_i \mathbf{c}_i f_i(\mathbf{x}, t)$.

The particle populations' evolution over time is expressed by the lattice Boltzmann equation that is usually divided into a collision and streaming step. The former reads

$$f_i^*(\mathbf{x}, t) = f_i(\mathbf{x}, t) + \Omega_i(\mathbf{x}, t) + S_i(\mathbf{x}, t). \quad (12)$$

Here, the post-collision distribution f_i^* is obtained using a collision operator Ω_i and an optional source term S_i . Furthermore, the propagation step with $\Delta t = \Delta x = 1$ is given by

$$f_i(\mathbf{x} + \mathbf{c}_i \Delta t, t + \Delta t) = f_i^*(\mathbf{x}, t), \quad (13)$$

which streams the particle populations to their corresponding neighboring lattice nodes.

The simplest way to account for collisions is to relax the distributions toward their equilibrium f_i^{eq} , as is done by the Bhatnagar–Gross–Krook (BGK) collision operator [28]

$$\Omega_i(\mathbf{x}, t) = -\omega(f_i(\mathbf{x}, t) - f_i^{\text{eq}}(\rho_f, \mathbf{u}_f)), \quad (14)$$

with the relaxation frequency ω that determines the speed of the relaxation and depends on the effective kinematic viscosity as follows

$$\omega = \left(3 \frac{\eta^*}{\rho_f} + \frac{1}{2} \right)^{-1}. \quad (15)$$

The Maxwell–Boltzmann distribution quantifying the equilibrium state reads [29]

$$f_i^{\text{eq}}(\rho_f, \mathbf{u}_f) = w_i \rho_f \left(1 + \frac{\mathbf{c}_i \cdot \mathbf{u}_f}{c_s^2} + \frac{(\mathbf{c}_i \cdot \mathbf{u}_f)^2}{2c_s^4} - \frac{\mathbf{u}_f^2}{2c_s^2} \right). \quad (16)$$

The required weights w_i originate from a Gauss–Hermite quadrature rule and are fixed for the chosen velocity set, as is the constant lattice speed of sound c_s . For D3Q19, the latter is $c_s = 1/\sqrt{3}$.

3.2 Integration of the truncated power law model

A truncated power law model is often used to consider non-Newtonian fluids with LBM. This ensures that the shear rate dependent local viscosity does not become too large or too small, causing instability or inaccuracy. Consequently, for Eq. (2), the following applies [30]

$$\eta^* = \max(\min(\tau_0 |\dot{\gamma}|^{-1} + k |\dot{\gamma}|^{n-1}, \eta_{\max}), \eta_{\min}). \quad (17)$$

The maximum and minimum viscosity η_{\max} and η_{\min} are predefined. In the following studies, we use $\eta_{\max} = 3$ and $\eta_{\min} = 3 \cdot 10^{-3}$. We emphasize that these are lattice units.

Therefore, the only unknown in Eq. (17) is the shear rate. To calculate it, it is advantageous that for non-forced LBM models the second momentum of the non-equilibrium part of the particle population f_i^{neq} and the shear rate tensor \mathbf{E} are related by [31]

$$\mathbf{E} = -\frac{\omega}{2\rho_f c_s^2} \sum_i f_i^{\text{neq}}(\rho_f, \mathbf{u}_f) \mathbf{c}_i \otimes \mathbf{c}_i. \quad (18)$$

Using the above, the shear rate is

$$\dot{\gamma} = \sqrt{2\mathbf{E} : \mathbf{E}}. \quad (19)$$

It should be noted that this method of calculating the shear rate has the advantage of being completely local.

3.3 Homogenized lattice Boltzmann method

In this work, we solve the particulate flow problem using the HLBM [32, 33], which uses a continuous model parameter, that can be seen as a confined permeability, $B(\mathbf{x}, t) \in [0, 1]$ to map rigid particles onto the entire computational domain [34–36]. By using the signed distance to the surface of the particle in this level set function, the method accommodates particles of any given shape [37].

The exact difference method (EDM) introduced by Kupershtokh et al. [38] is adapted to account for the influence of the particles on the fluid [35], which introduces the following source term in Eq. (12)

$$S_i(\mathbf{x}, t) = f_i^{\text{eq}}(\rho_f, \mathbf{u}_f + \Delta\mathbf{u}_f) - f_i^{\text{eq}}(\rho_f, \mathbf{u}_f). \quad (20)$$

Using a convex combination of fluid and particle velocities [35]

$$\Delta\mathbf{u}_f(\mathbf{x}, t) = B(\mathbf{x}, t) (\mathbf{u}_p(\mathbf{x}, t) - \mathbf{u}_f(\mathbf{x}, t)), \quad (21)$$

the velocity difference $\Delta\mathbf{u}_f(\mathbf{x}, t)$ is obtained. The coupling from the fluid to the particles follows Wen et al. [39], leading to the local hydrodynamic force

$$\mathbf{F}_h(\mathbf{x}, t) = \sum_i (\mathbf{c}_i - \mathbf{u}_p(\mathbf{x}, t)) f_i(\mathbf{x} + \mathbf{c}_i, t) + (\mathbf{c}_i + \mathbf{u}_p(\mathbf{x}, t)) f_i^-(\mathbf{x}, t). \quad (22)$$

The integral hydrodynamic force is calculated by aggregating the local forces occurring at all nodes within the particle. These nodes are represented by the position vector \mathbf{x}_b . Thus, the resulting total hydrodynamic force is expressed as

$$\mathbf{F}_p(t) = \sum_{\mathbf{x}_b} \mathbf{F}_h(\mathbf{x}_b, t). \quad (23)$$

The torque is governed by

$$\mathbf{T}_p(t) = \sum_{\mathbf{x}_b} (\mathbf{x}_b - \mathbf{X}_p) \times \mathbf{F}_h(\mathbf{x}_b, t). \quad (24)$$

3.4 Discrete contacts

The particle-fluid coupling process performs a preliminary contact detection by evaluating the particle distances at each node. If the distance between two particles is less than half the cell diagonal ($d_s < \sqrt{0.75}\Delta x$), a contact is assumed and an initial approximate cuboid or bounding box is formed around the contact area. This bounding box serves as the domain for iterative calculations to determine the parameters necessary to compute the contact forces, including the overlap volume, the indentation depth, and the contact normal. However, the relatively large lattice spacing often results in an inaccurate bounding box due to insufficient overlap resolution. To compensate for this, a refinement step is performed by iterating over the surface of the initial approximation using a specified number of points in each spatial direction, known as the contact resolution N_c . In this paper we use $N_c = 7$. The distance to the actual contact is calculated at each point in discrete directions, increasing the precision of the bounding box. Finally, the contact resolution N_c is used to iterate over the entire overlap region, determining the overlap volume, contact point, contact normal, indentation depth, and contact force. For a complete understanding of the algorithm, please refer to the corresponding publication [40, 41].

4 Setups

4.1 Dimensionless Numbers

In the context of a suspension containing fruit particles and a Herschel–Bulkley fluid flowing through a constricted cross-section as shown in Fig. 1, the following dimensionless quantities are derived using the Pi theorem:

$$\begin{aligned}
 \bullet \Pi_1 &= \text{Re} = \frac{\rho_f D^n \bar{u}^{2-n}}{K} & \bullet \Pi_7 &= \frac{D_p}{D} \\
 \bullet \Pi_2 &= \alpha & \bullet \Pi_8 &= \frac{d}{D} = 0.5 \\
 \bullet \Pi_3 &= n & \bullet \Pi_9 &= \frac{\rho_p}{\rho_f} = 1 \\
 \bullet \Pi_4 &= \nu & \bullet \Pi_\sigma &= \frac{\sigma}{\bar{u}^2 \rho_f} \\
 \bullet \Pi_5 &= \phi_p & \bullet \Pi_F &= \frac{F}{\bar{u}^2 D^2 \rho_f} \\
 \bullet \Pi_6 &= \frac{\Delta p}{\bar{u}^2 \rho_f}
 \end{aligned}$$

Π_1 is the Metzner–Reed Reynolds number [42]. The last two mentioned dimensionless quantities apply to all stresses σ and elasticity modules E (Π_σ) as well as forces F (Π_F). To avoid repetition, however, the quantities have only been listed once. Furthermore, \bar{u} refers to the average velocity of the suspension, α to the taper angle, and D_p to the particle size as the diameter of a volume-equivalent sphere.

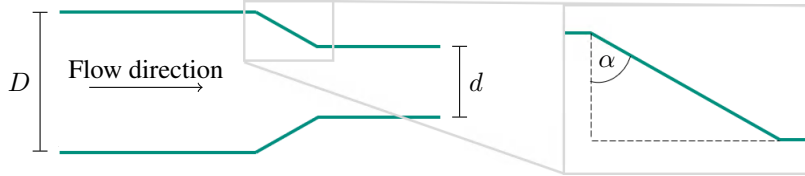


Figure 1: Sketch of the abstract geometry showing flow direction and geometric parameters.

4.2 Experimental

Preparation of the model fluids The preparation of the model fluids is done in three steps. The preparation of liquid and the particulate phase, followed by a mixing step. The liquid phase consists of 23% sucrose, 1.169% NaCl, 0.924% sodium carboxymethyl cellulose, and 0.0616% Laponite as a rheology additive to implement a yield point. First, the sucrose, the carboxymethyl cellulose, and the NaCl are homogenized into distilled water at 60 °C. The carboxymethyl cellulose solution is then left 24 h for hydration. Then, the Laponite solution is blended in a ratio of 3 : 2.

The particulate phase is represented by hydrocolloid gels from 1.106% κ -Carrageenan and 1.169% NaCl to imitate the material characteristics of the fruit pieces. 20.5% Sucrose is added to adjust the density and refractive index matching, necessary for the usage in PIV experiments. To prepare the gels, the mixture was heated for 30 min to 65 °C and subsequently stored for gelation in 5 L buckets for 24 h at 7 °C. After the gelation the gel is cut into cubes of approximately 10 × 10 × 10 mm and carefully mixed by hand with the liquid phase, adjusting the particle mass fraction to 30%.

Rheological Analysis of the liquid phase Firstly, the yield points of the liquid phases are determined through an amplitude sweep. For this purpose, an MCR 102 Rheometer (Anton Paar GmbH, Graz, Austria) with a CP50-1 cone-plate measuring geometry is used. The measurement is conducted under shear rate control, with a shear strain ranging from 0.01% to 100% at a frequency of $f = 10 \text{ rad s}^{-1}$. After determining the yield points, flow curves of the samples are created. Hence, the samples are measured utilizing a controlled shear rate protocol consisting of four sections. In the first section, pre-shearing is conducted for 60 s at a shear rate of $\dot{\gamma} = 0.1 \text{ s}^{-1}$. In the second section, a linear shear rate ramp from 0.1 to 250 s^{-1} is applied. The third section involved a holding time of 60 s at a shear rate of 250 s^{-1} , while in the fourth section, a downward ramp from 250 to 0.1 s^{-1} is applied. The evaluation of the measurement data is performed in MATLAB (The MathWorks, Inc, Natick, USA). Here, the measurement data of the downward ramp is utilized to determine the parameters of the nonlinear Herschel–Bulkley model, see Eq. (2), using the method of least squares.

Mechanical Testing For optical flow measurements, imitates of the fruit pieces were created. These imitates showed a similar mechanical behavior as peach samples from fruit preparations without mimicking the anisotropic behavior

[43, 44]. These hydrogels allow an extensive mechanical testing, since defined probes can be created. This is used to determine the end of the linear elastic range and the end of the viscoelastic range in uniaxial compression that is needed for the determination of the damage potential as described in 4.3. To characterize the mechanical behavior of the hydrogel samples, an uniaxial compression test is performed with a Z 1.0 (Zwick/Roell GmbH & Co. KG, Ulm, Germany) testing machine. A 50 mm diameter compression plate is attached to a Xforce P (5 N) force transducer with a maximum load of 1 kN. The tests are carried out with a preload force of 0.1 N. A sheet of paper is placed under the sample, creating friction between the material and the rigid support to avoid slipping. Each sample is compressed to failure to register its strength and strain. A preload force of 0.1 N is reached with a velocity of 15 mm min^{-1} . Then, the gel sample is compressed with a speed of 5 mm min^{-1} until the desired tool distance is reached.

Flow channel The experimental setup shown in Fig. 2 consists of tank 1 (1), a pneumatic ball valve (2) (FESTO, Esslingen am Neckar, Germany), an inlet section (3) with a length of 75.11 cm, the measurement geometry (4), a magnetic-inductive flow meter (5) (MID) of the type Promag H300 (Endress + Hauser, Reinach, Switzerland), and tank 2 (6). The two tanks each have a total volume of 100 L. They are equipped with two level sensors to prevent overfilling and air ingress into the pipeline. For this purpose, the level sensors are coupled to the ball valve via a relay circuit. The ball valve is only used to open and close the pipeline and not as a control valve. The flow rate is controlled by pressurizing tank 1 using a PID controller. For this purpose, an EL-PRESS pressure measuring and control valve (7) (Bronkhorst High-Tech B.V., Ruurlo, Netherlands) is integrated in a cascade circuit in LabVIEW (National Instruments, Austin, United States). The experiments are recorded with a Mini Ax 100 (Photron, Tokyo, Japan) high-speed camera operated in the DaVis (LaVision GmbH, Göttingen, Germany) PIV imaging software.

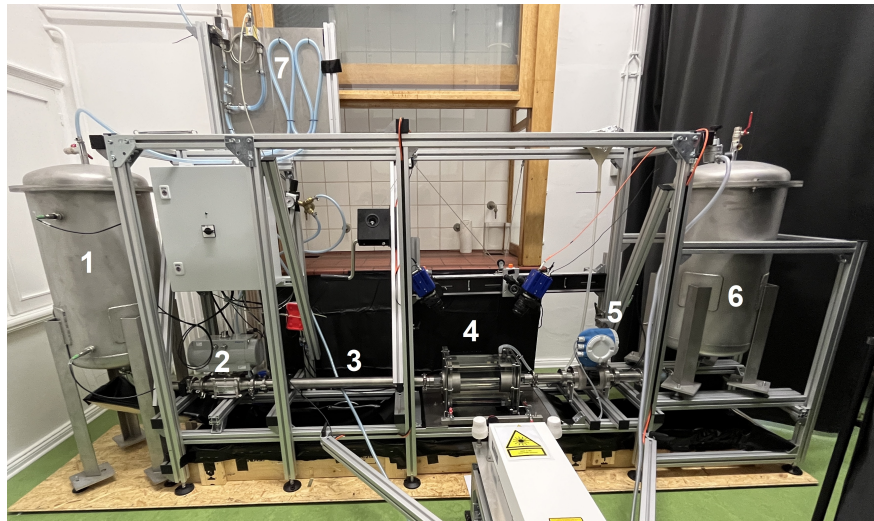


Figure 2: Experiment for the evaluation of the damage potential of different pipe geometries.

Pipe Geometries A total of three pipe geometries are used. In order to validate the numerical simulations, a straight pipe with a diameter of 50 mm and a sudden and gradual cross-sectional change from 50 mm to 25 mm are investigated. Sketches of the pipe geometries are shown in Fig. 3.

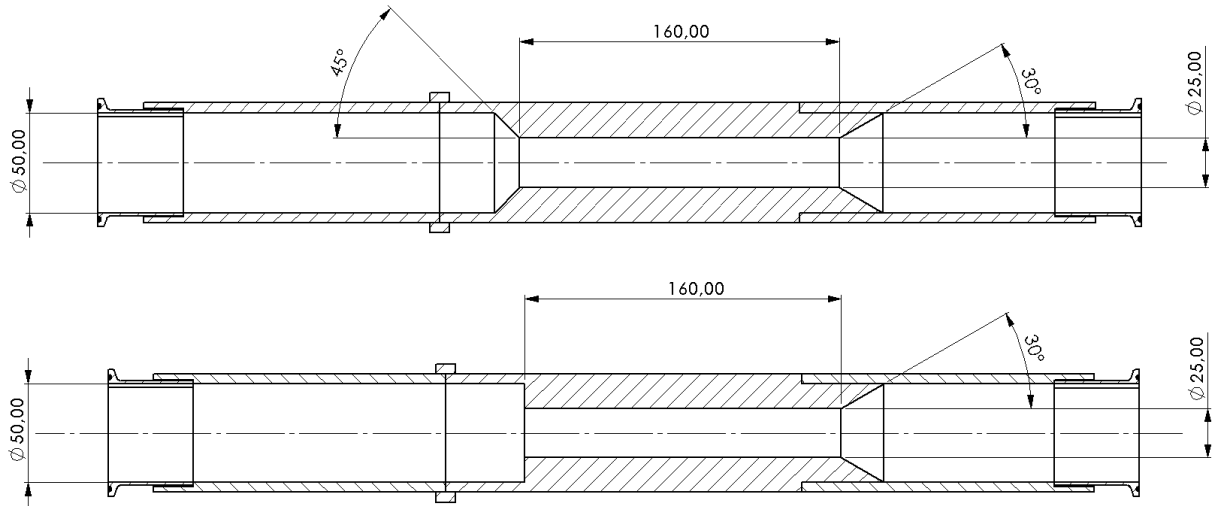


Figure 3: Experiment for the evaluation of the damage potential of different pipe geometries.

Flow Experiments Approximately 50 L of industrial fruit preparation and model fluid are passed through the geometries in 20 runs each. Particle size distribution is determined before and after the experiments in triplicates. For each experiment, a fresh sample is taken, and the fruit preparations are conveyed at rates of 20 L min^{-1} and 40 L min^{-1} . Thus, Reynolds numbers of $Re = 2$ and $Re = 5$ are set for pipe diameters of 50 mm. Due to high effort for their preparation, the model fluids are conveyed at volume flow rates of 20 L min^{-1} , to achieve $Re = 5$.

Determination of particle size distribution The particle size distribution of the fruit preparations is determined in triple determination using wet sieving. Sieving is performed using an Analysette sieve tower (Fritsch GmbH, Idar-Oberstein, Germany) and six sieves (mesh sizes: 8, 6.3, 5, 4, 2, and 1 mm). 500 g of the fruit preparation is sieved with an amplitude of 2 mm for three minutes. The material is sieved wet for two minutes and dry for one minute. Spraying, at a flow rate of 1.4 L min^{-1} at $40 \text{ }^\circ\text{C}$, is achieved using a sieve cover with three spray nozzles. The liquid is drained through a sieve tray with an outlet. Subsequently, the sieves are set up at an angle of 45° for five minutes to allow the remaining water to drain off. The weight of each fraction is then determined.

The particle size distribution of the model particles is determined by the analysis of images of samples in Petri dishes. For every conveying experiment, 20 Petri dishes are filled with sample and pictures are recorded using a Nikon COOLPIX P7700 (Nikon, Tokio, Japan) digital camera. The upper surfaces of the containing particles are determined using ImageJ (NIH, Bethesda, USA) where the measured area is cropped for traceability reasons. Altogether 1741 particles are measured, an example of the procedure is shown in Fig. 4. The number of measured particles (n_p) ranges from 417 – 467 per experiment.

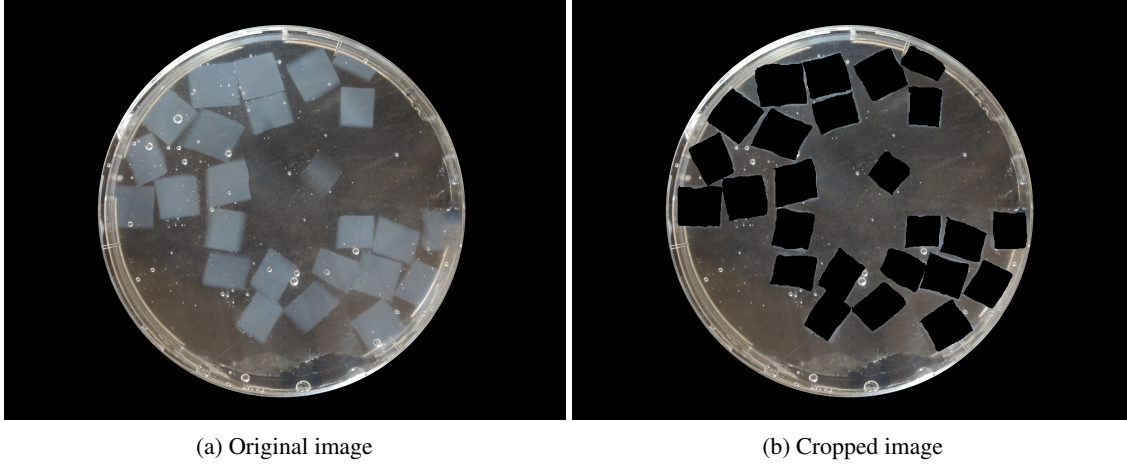


Figure 4: Example for the measurement of the model particles before and after the experiments.

4.3 Computational

In this section, the simulation setup is described, focusing on the geometry, studied parameters, discretization, boundary and initial conditions and employed.

Geometry The simulations focus on the constriction of the cross-section. The diameter at the inlet is set to $D = 50$ mm and is reduced to $D/2$ in the second part. The transition section is characterized by the taper angle α , as shown in Fig. 1. Here, $\alpha = 0^\circ$ represents an abrupt change in cross-section, while $\alpha = 90^\circ$ describes a straight pipe. The total length of the pipe is $10D$, with the left part comprising 70% to ensure sufficient particle delivery. For $\alpha < 90^\circ$, the conical narrowing length is given by $D/4 \tan \alpha$.

Physical Parameters The main parameters of investigation are the Reynolds number $Re \in \{2, 3, 5, 8\}$ and the taper angle $\alpha \in \{0, \frac{\pi}{8}, \frac{\pi}{4}, \frac{3\pi}{8}, \frac{\pi}{2}\}$. The decision to focus on these specific parameters is based on the practical importance of avoiding changes in the formulation of the product for consumer acceptance. The mechanical properties of fruit preparations depend on a number of factors, including season, degree of processing, and recipe. As a result, they are not easily adjusted. Varying the Reynolds number, on the other hand, allows analysis of the effects of different speeds on stress, making it a crucial adjustable parameter during plant design. Similarly, the angle of cross-sectional change can be adjusted during design. The non-Newtonian fluid is modeled as a Herschel–Bulkley fluid, with flow index $n = 0.42$, consistency $K = 13.1 \text{ Pa s}^{0.42}$, and density $\rho_f = 1100 \text{ kg m}^{-3}$. Particles are immersed in the fluid with a particle volume fraction $\phi_p \approx 0.3$. The cubic particles vary in size, i.e. $\Pi_7 \in \{0.159, 0.2\}$, and have a Poisson’s ratio $\nu = 0.3$, consistent with data reported on apples [45], and two Young’s moduli of 30 kPa and 60 kPa, corresponding to those of the model particles and the considered fruit particles. The steel walls have an elastic modulus of 190 GPa and a Poisson’s ratio of 0.3 [46]. Gravity is neglected due to the similar density of the fluid and particles, and $\rho_p = \rho_f$ is assumed. The restitution coefficient in the simulations is 0.9, the static friction coefficient is 0.15 [47], and the sliding friction coefficient is 0.1.

Discretization During the simulation, the inlet diameter is resolved with N grid points, thus $\Delta x = D/N$. In case of contacts, the contact region resolution is $N_c = 7$. The time step size is $\Delta t = 5 \mu\text{s}$.

Boundary Conditions A constant velocity field is prescribed at the inlet, with no-slip conditions at the walls and a constant pressure at the outlet. To obtain the velocity profile, a preliminary simulation in a straight pipe of length $6D$ is conducted, with a constant inlet velocity corresponding to the mean flow velocity \bar{u} . The established flow profile at $x = 4.5D$ is used as a boundary condition for subsequent simulations with the same fluid parameters. The velocity and pressure boundaries are realized using the regularized method according to Latt and Chopard [48], while the no-slip boundary condition on the curved stationary wall follows Bouzidi *et al.* [49].

Initial Conditions To limit the computational intensity of particle-laden simulations, the fluid velocity field is first computed without particles and then used as initial conditions for simulations including particles. Particles inherit the fluid velocity at their center of mass. The total simulation time is 1.1 s, with the first 0.1 s used to smooth initial gradients resulting from the particles being initialized without rotation. Since the initial particle distribution is unpredictable,

random particle positions are generated to achieve a homogeneous distribution, as observed in experiments from tanks and desired in industrial applications. The initial distributions in a periodic pipe of length $7D - D_p$ are shown in Fig. 5. The length is chosen to match the front section's length, with the reduction by the particle diameter avoiding significant overlaps with boundaries at the start of the subsequent simulations.

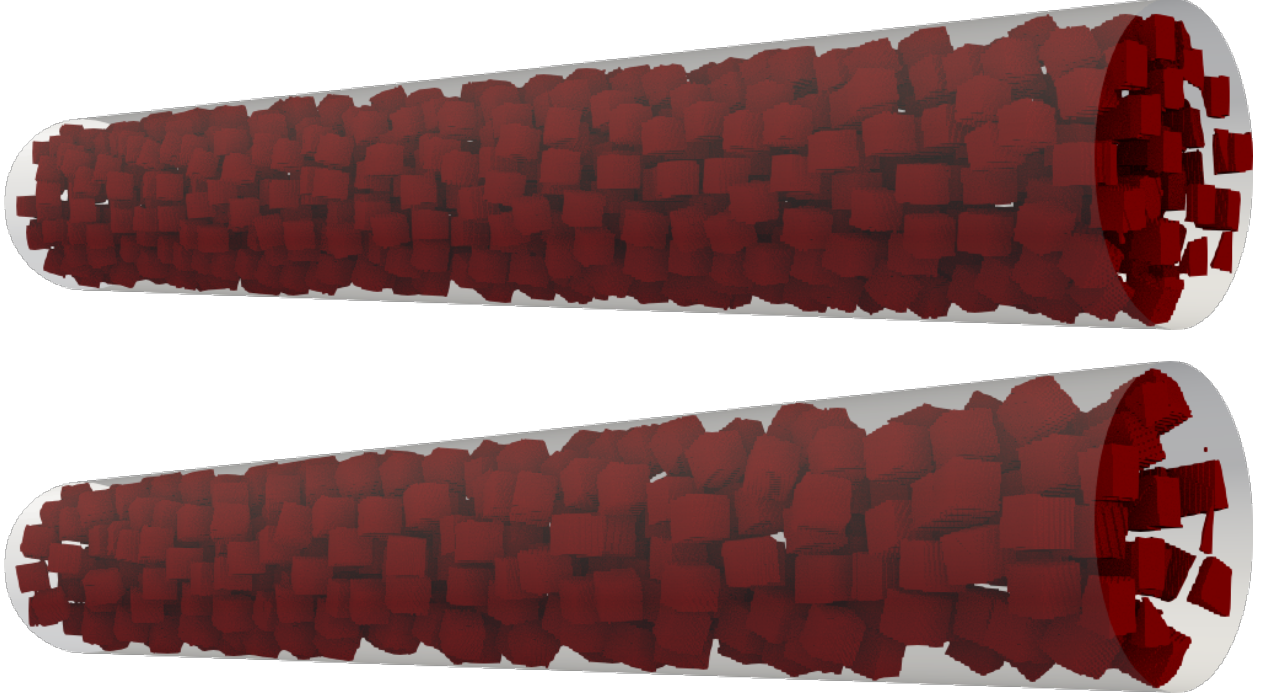


Figure 5: Visualization of the initial fruit particle distributions using a resolution $N = 131$ for $\Pi_7 = 0.159$ (top) and $\Pi_7 = 0.2$ (bottom).

Damage potential In the following, the potential for damage to the particle component is quantified by

$$DP = \frac{1}{n} \sum_{j=1}^n \begin{cases} 1 & \text{for } \sigma_j \geq \sigma_v \\ \frac{\sigma_v - \sigma_j}{\sigma_v - \sigma_1} & \text{for } \sigma_1 \leq \sigma_j < \sigma_v \\ 0 & \text{for } \sigma_j < \sigma_1 \end{cases} . \quad (25)$$

The damage potential indicates the probability of damage. For this purpose, the probability of damage per data point j is determined. Subsequently, these are summed up and divided by the total number of data points n . Here, the experimental data described in Section 4.2 and shown in Table 1 is used. For stresses within the linear elastic range ($\sigma_j < \sigma_1$), it is assumed that no damage occurs, above the viscoelastic range ($\sigma_j \geq \sigma_v$), damage is always assumed to occur. In the viscoelastic range, the gradual transition is approximated by a linear progression. The aforementioned damage potential is evaluated for each type of stress, i.e. normal and tangential stress due to interaction with the fluid as well as normal and tangential stress due to contact with other particles and walls.

Grid independence In the grid independence study we consider $\alpha = 45^\circ$, $Re = 5$, $\Pi_7 = 0.2$, $E = 30$ kPa, and $N \in \{81, 91, 101, 111, 121, 131, 141\}$. These resolutions are compared to a baseline resolution of $N = 151$ to confirm grid independence. The results are visualized in Fig. 6, which shows the relative error of the damage potentials, calculated using the L^2 norm as described in [26], plotted against the different grid resolutions. In the figure, circles represent the fluid-induced normal (FIN) stress, squares represent the fluid-induced tangential (FIT) stress, triangles represent the contact-induced normal (CIN) stress, and diamonds represent the contact-induced tangential (CIT) stress as the corresponding causes of the damage potential. In addition, the figure includes lines denoting experimental orders of convergence with values of 1 and 2. It can be seen that, in general, the error decreases with increasing resolution, more closely following the line for EOC = 2. The relative error falls below 10% for all damage potentials for $N \geq 131$. Therefore, $N = 131$ is chosen for the following studies. It is also noteworthy that the error for the damage potential due to CIT stresses is generally higher due to their lower values, as can be seen in Section 5.2.

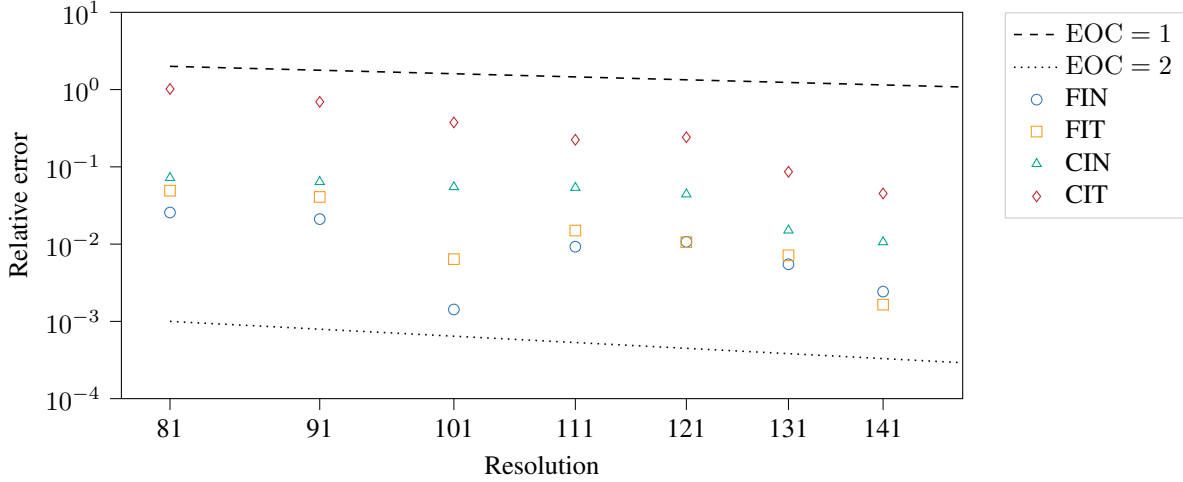


Figure 6: Relative error of the FIN, FIT, CIN, and CIT damage potential in L^2 norm versus the reference resolution $N = 151$.

5 Results

This section presents the results of our research, including both experimental and computational results. We begin in Section 5.1 with the results of our experiments, providing an analysis of the data collected. Then, in Section 5.2, we turn our attention to the computational results, exploring the results of our simulations and their implications. Next, in Section 5.3, we validate our experimental and computational results by comparison, establishing the reliability and consistency of our findings. In the discussion that follows in Section 5.4, we interpret the results, compare experimental and computational data, and consider the broader context of our findings within the field.

5.1 Experimental

Rheological Analysis of the liquid phase The fitting of the Herschel–Bulkley model resulted in the following parameters for the fluid of the Fruit preparations. The yield stress is $\tau_0 = 0.653$ Pa, the flow index is $n = 0.42$, and the consistency is $K = 13.1$ Pa s^{0.42}. The yield stress of the model fluid is $\tau_0 = 0.244$ Pa, the flow index is $n = 0.512$, and the consistency is $K = 2.934$ Pa s^{0.512}.

Mechanical Testing The results of the mechanical testing are shown in Table 1. The stress limits of the linear elastic and viscoelastic ranges are used to determine the damage potential as described in Section 4.3.

Table 1: Mechanical behavior of the hydrogel.

Limit	Strain in %	Stress in kPa
Linear elastic	6.50 ± 0.47	2.228 ± 0.258
Viscoelastic	22.06 ± 2.02	13.47 ± 1.60
Failure	30.58 ± 2.47	20.27 ± 6.09

Damage Investigation Example images of the recorded footage are shown Figs. 7 and 8. It was observed, that the fruit preparation’s turbidity increased during the experiment, hampering the identification of the particle shape. It appears that the share of small particles expanded, but it can be seen that the recordings can exclusively be used for a subjective interpretation of the particle damaging. For the objective analysis, wet sieving is necessary. As it can be seen in Fig. 8 the distinction of the model particles is not possible from the image material. Since the model particles are designed for PIV experiments, their transparent nature obstructs the inline assessment of the particle size. Further experiments showed that wet sieving also was not applicable to the model fluids, since the hydrogel particles were washed out during the wet sieving process. Therefore, the particle size of the model particles was determined by images

of the Petri dishes filled with samples, that were collected after the experiment as described in Section 4.2.

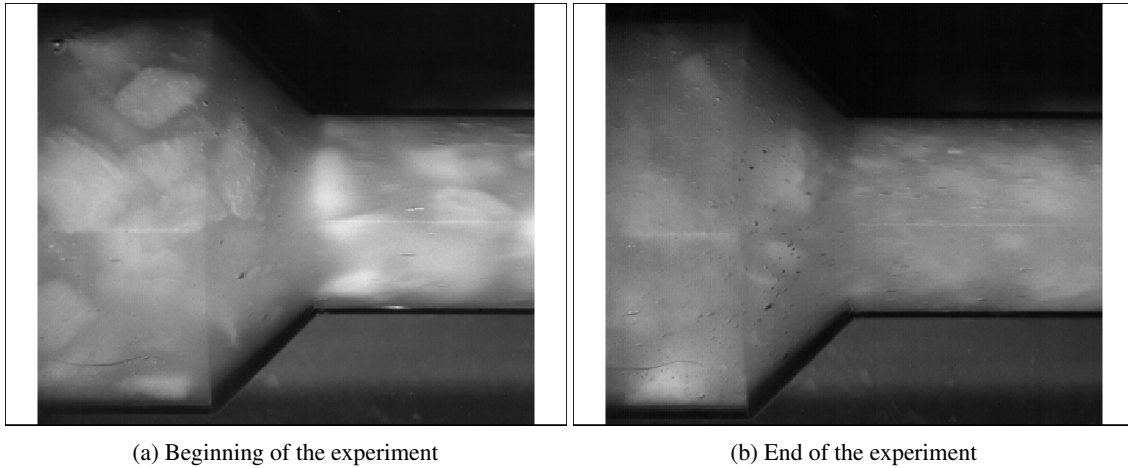


Figure 7: Images taken during the conveying experiment with fruit preparations in a smooth constriction and a volume flow of 40 L min^{-1} .

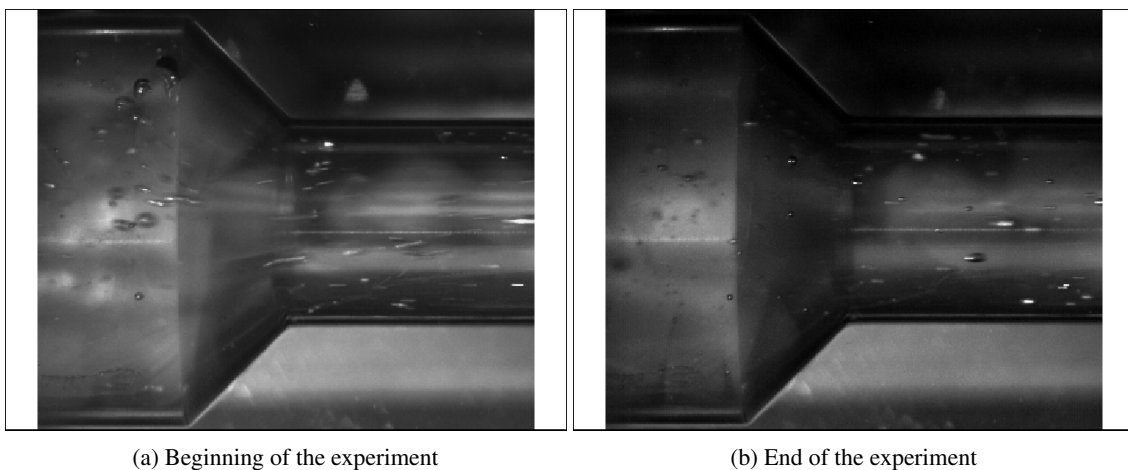


Figure 8: Images taken during the conveying experiment with the model fluids in a smooth constriction and a volume flow of 20 L min^{-1} .

The results of the damage investigation of the fruit preparations are shown in Figs. 9 to 11. These experiments are done to compare with the numerical results for the damage potential shown in Tables 2 to 5. It can be observed that in the experiments with a flow rate of 20 L min^{-1} ($Re = 1.46$), the particle size distribution is comparable to that of the unconveyed sample. The experiments with a flow rate of 40 L min^{-1} ($Re = 4.4$) resulted in a significant reduction of fractions above 6.3 mm , both in steady and sudden cross-sectional narrowing, with the fraction at 5 mm increasing. This cannot be seen in the straight pipe. Thus, it can be said that the change in cross-section induces damage to the fruit pieces. However, the different types of cross-sectional changes appear to have only a minor influence on the extent of damage. This confirms that the angle of narrowing has a minor impact on the damage potential of the fruit pieces. The experiments also indicate that the damage potential increases with increasing $\Pi_7 = D_p/D$, leading to a decrease in fractions of larger particles.

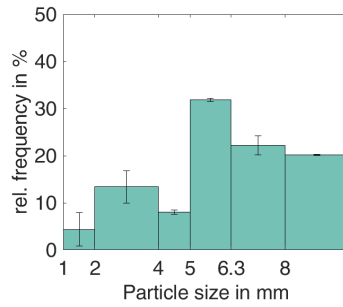
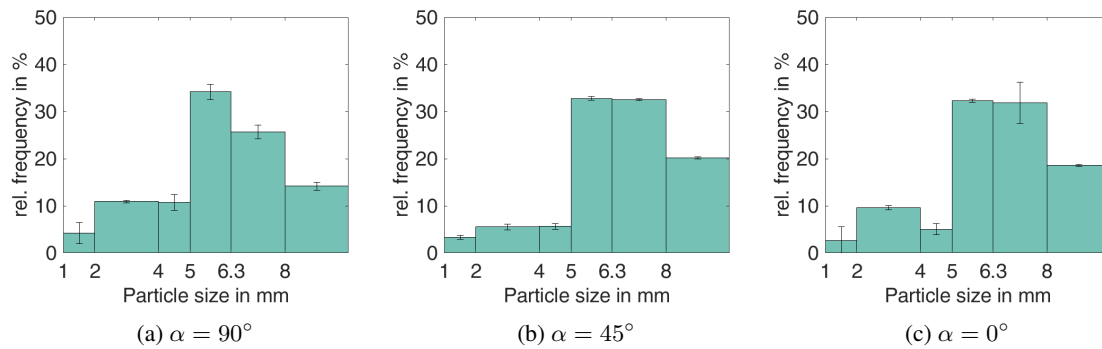
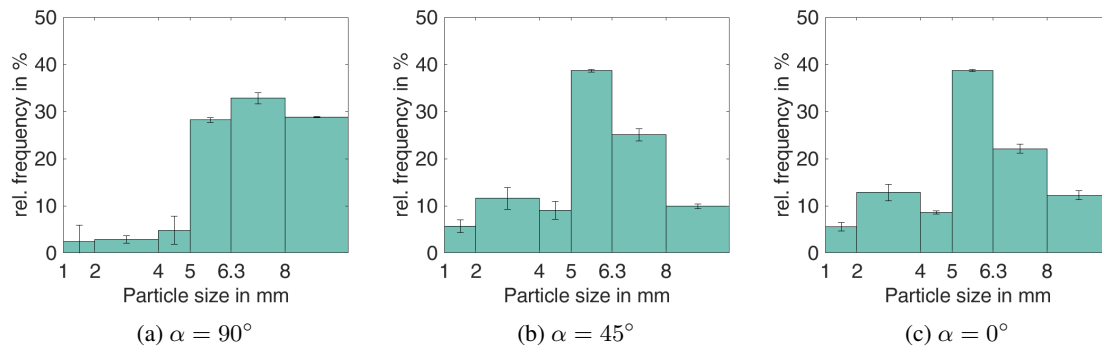
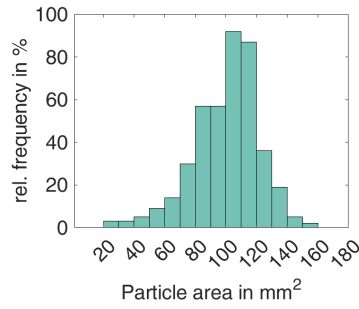
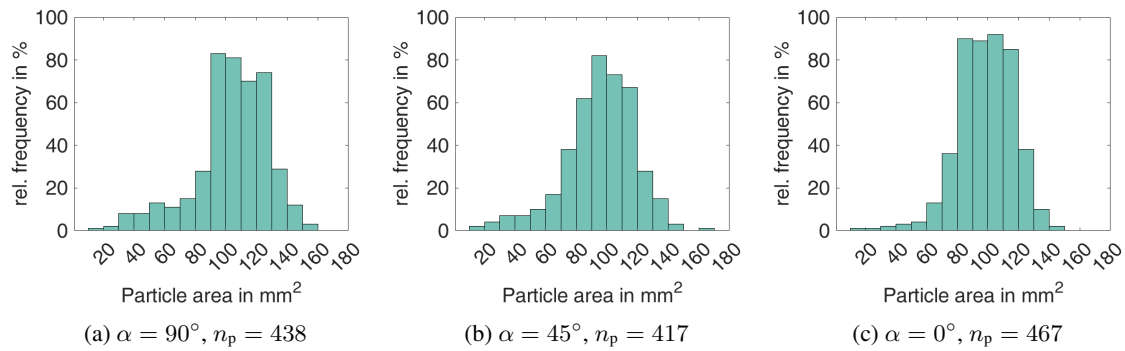


Figure 9: Initial particle distribution.

Figure 10: Particle distribution after experiments with a flow rate of 20 L min⁻¹.Figure 11: Particle distribution after experiments with a flow rate of 40 L min⁻¹.

In Figs. 12 and 13 the results for the experiments with the model particles at a volume flow rate of 20 L min⁻¹ ($Re = 5.78$) are shown. Since wet sieving was not applicable on the model particles, the histograms show the area of the upper surface of the particles. The model particles show comparable damaging as the fruit particles. Since the model particles were cut by hand into cubes, they show a narrow particle size distribution, with the majority of upper surface areas between 70 – 130 mm². After the conveying in the geometry with $\alpha = 90^\circ$ the fraction between 90 – 100 mm² shows higher counts than before. Conveying through the geometry with $\alpha = 45^\circ$ leads to a widening of the distribution with a peak in the fraction between 90 – 100 mm², whereas the geometry with $\alpha = 0^\circ$ leads to a further increased in the fraction between 90 – 100 mm².

Figure 12: Initial particle distribution $n_p = 419$.Figure 13: Particle size distribution of the model particles after the experiments with a flow rate of 20 L min^{-1} . With n_p as number of the measured particles.

5.2 Computational

The results of the simulation with $Re = 5$, $\alpha = 45^\circ$, $\Pi_7 = 0.2$, $E = 30 \text{ kPa}$, and $N = 131$ are given in Figs. 14 to 17, showing the average distance to the center of the pipe in Fig. 14, number of particle-particle and particle-wall contacts in Fig. 15, fluid-induced stress in Fig. 16, and contact-induced stress in Fig. 17 versus the length of the pipe. The plots in Figs. 16 and 17 show the median of the induced stresses as a line next to the range that includes 90% of the data, shown as an area. This range excludes the 5% lowest and 5% highest stresses to highlight trends while minimizing the impact of outliers.

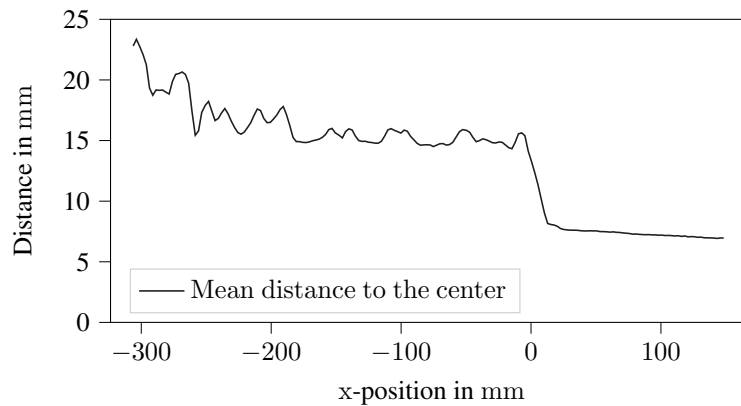


Figure 14: Plot of the average distance to the center of the pipe versus the length of the pipe.

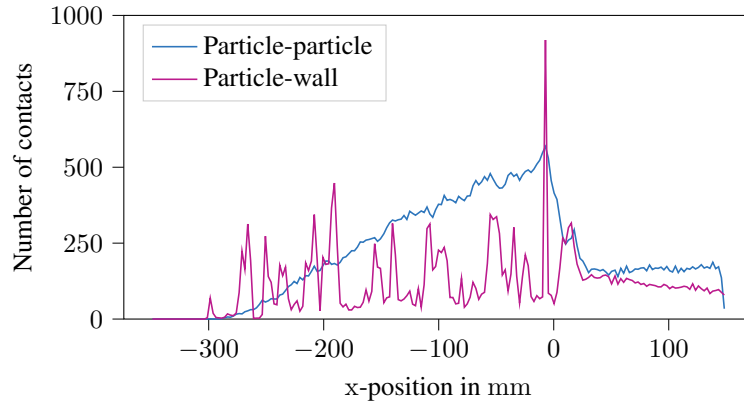


Figure 15: Plot of the number of contacts versus the length of the pipe.

Fig. 14 indicates that the motion of particles is directed towards the central point of the pipe, due to the narrowing of the pipe's cross-section. This leads to a rise in the frequency of particle-to-particle interactions, as visible in Fig. 15, as they undergo repositioning in the path leading to the constriction, and subsequently maintain a steady level of contact. Furthermore, instances of particle-wall contacts are most prevalent at the onset of the constriction and the area preceding it, and decrease in the section with a smaller diameter.

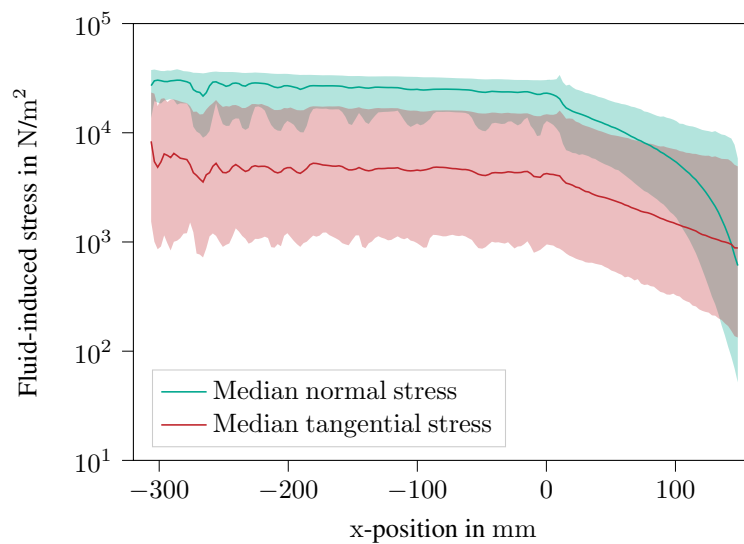


Figure 16: Plot of the fluid-induced stress versus the length of the pipe.

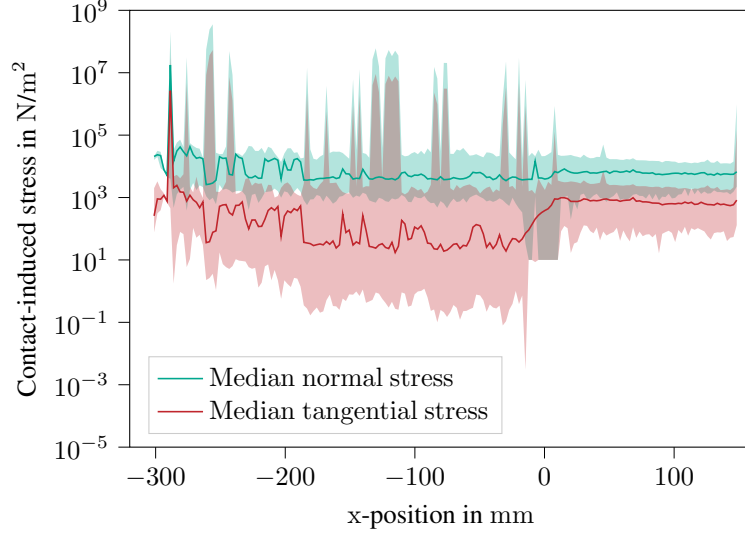


Figure 17: Plot of the contact-induced stress versus the length of the pipe.

Examining the Figs. 16 and 17, it is evident that the normal stresses exceed the tangential component in magnitude. After the constriction, the fluid-induced stresses decrease in intensity, while the normal stresses caused by the contacts remain at a comparable level. In addition, an increase in the tangential stresses caused by contact is observed, which can be attributed to the higher relative velocities involved.

Tables 2 to 5 show the damage potential of the fluid-induced normal (FIN), fluid-induced tangential (FIT), contact-induced normal (CIN), contact-induced tangential (CIT) stresses for $Re \in \{2, 3, 5, 8\}$, $\alpha \in \{0, \frac{\pi}{8}, \frac{\pi}{4}, \frac{3\pi}{8}, \frac{\pi}{2}\}$, expressed in radians, $\Pi_7 \in \{0.159, 0.2\}$, $E = 30$ kPa, and $E = 60$ kPa.

Table 2: Damage potential of FIN, FIT, CIN, CIT stress for $\Pi_7 = 0.159$ and $E = 30$ kPa.

α	$Re = 2$				$Re = 3$			
	FIN	FIT	CIN	CIT	FIN	FIT	CIN	CIT
0°	0.807	0.489	0.592	0.081	0.848	0.522	0.605	0.070
22.5°	0.800	0.485	0.595	0.076	0.853	0.523	0.606	0.071
45°	0.763	0.471	0.590	0.079	0.838	0.510	0.598	0.073
67.5°	0.680	0.442	0.585	0.078	0.783	0.481	0.599	0.071
90°	0.453	0.210	0.574	0.098	0.474	0.205	0.582	0.080
α	$Re = 5$				$Re = 8$			
	FIN	FIT	CIN	CIT	FIN	FIT	CIN	CIT
0°	0.878	0.553	0.626	0.062	0.905	0.572	0.658	0.058
22.5°	0.882	0.554	0.632	0.068	0.904	0.574	0.652	0.068
45°	0.877	0.551	0.621	0.062	0.905	0.576	0.649	0.066
67.5°	0.866	0.542	0.621	0.059	0.908	0.577	0.661	0.063
90°	0.489	0.239	0.592	0.061	0.501	0.277	0.605	0.052

Table 3: Damage potential of FIN, FIT, CIN, CIT stress for $\Pi_7 = 0.2$ and $E = 30$ kPa.

α	$Re = 2$				$Re = 3$			
	FIN	FIT	CIN	CIT	FIN	FIT	CIN	CIT
0°	0.807	0.482	0.618	0.063	0.842	0.513	0.642	0.059
22.5°	0.802	0.481	0.607	0.060	0.858	0.520	0.619	0.063
45°	0.778	0.474	0.608	0.063	0.846	0.511	0.622	0.056
67.5°	0.667	0.432	0.603	0.071	0.794	0.485	0.623	0.060
90°	0.452	0.167	0.585	0.093	0.491	0.178	0.587	0.074

α	$Re = 5$				$Re = 8$			
	FIN	FIT	CIN	CIT	FIN	FIT	CIN	CIT
0°	0.880	0.546	0.657	0.065	0.905	0.566	0.661	0.063
22.5°	0.881	0.549	0.656	0.068	0.906	0.568	0.666	0.071
45°	0.879	0.547	0.659	0.060	0.907	0.569	0.666	0.057
67.5°	0.871	0.545	0.656	0.056	0.907	0.567	0.685	0.062
90°	0.496	0.216	0.592	0.058	0.499	0.256	0.608	0.055

Table 4: Damage potential of FIN, FIT, CIN, CIT stress for $\Pi_7 = 0.159$ and $E = 60$ kPa.

α	$Re = 2$				$Re = 3$			
	FIN	FIT	CIN	CIT	FIN	FIT	CIN	CIT
0°	0.746	0.447	0.613	0.147	0.850	0.521	0.621	0.146
22.5°	0.714	0.440	0.614	0.149	0.838	0.510	0.622	0.145
45°	0.669	0.426	0.614	0.153	0.840	0.512	0.623	0.152
67.5°	0.558	0.389	0.612	0.157	0.783	0.476	0.623	0.146
90°	0.707	0.319	0.621	0.148	0.758	0.366	0.629	0.149

α	$Re = 5$				$Re = 8$			
	FIN	FIT	CIN	CIT	FIN	FIT	CIN	CIT
0°	0.885	0.550	0.643	0.152	0.915	0.579	0.684	0.139
22.5°	0.885	0.554	0.643	0.155	0.916	0.579	0.696	0.137
45°	0.885	0.555	0.638	0.153	0.917	0.578	0.685	0.140
67.5°	0.872	0.549	0.631	0.142	0.912	0.577	0.680	0.137
90°	0.780	0.401	0.652	0.153	0.782	0.434	0.674	0.144

Table 5: Damage potential of FIN, FIT, CIN, CIT stress for $\Pi_7 = 0.2$ and $E = 60$ kPa.

α	$Re = 2$				$Re = 3$			
	FIN	FIT	CIN	CIT	FIN	FIT	CIN	CIT
0°	0.839	0.507	0.647	0.156	0.869	0.531	0.648	0.157
22.5°	0.827	0.501	0.646	0.156	0.873	0.533	0.652	0.161
45°	0.803	0.488	0.639	0.163	0.871	0.531	0.651	0.163
67.5°	0.680	0.430	0.632	0.153	0.817	0.496	0.646	0.148
90°	0.689	0.295	0.641	0.173	0.723	0.329	0.649	0.167

α	$Re = 5$				$Re = 8$			
	FIN	FIT	CIN	CIT	FIN	FIT	CIN	CIT
0°	0.878	0.541	0.674	0.150	0.914	0.570	0.726	0.141
22.5°	0.883	0.547	0.667	0.157	0.917	0.573	0.716	0.145
45°	0.886	0.551	0.663	0.161	0.917	0.570	0.718	0.146
67.5°	0.878	0.550	0.656	0.158	0.913	0.572	0.715	0.138
90°	0.734	0.364	0.672	0.159	0.753	0.410	0.692	0.154

In general, the damage potential of FIN stresses is the highest, followed by CIN stresses and FIT stresses. All these stresses are on a similar relatively high level, only the CIT stresses have a minor damage potential.

Furthermore, the damage potential for all stresses increases with Re . This trend is consistent across all the tables and angles. The increase in damage potential with Re is more pronounced for FIN and FIT stresses than for CIN and CIT stresses.

The damage potential for FIN, FIT, CIN, and CIT stresses also varies with the angle α . For $Re \leq 3$, the angle, especially for $\alpha \geq 67.5^\circ$, has higher influence than for $Re \geq 5$. However, in across all parameters, a big difference in FIN and FIT stresses is observed for $\alpha = 90^\circ$, i.e. a pipe without any cross-section constriction. This is also observed for the damage potential due to CIN stresses, but only for $E = 30$ kPa, for $E = 60$ kPa those differences vanish.

The changes to the damage potential for FIN and FIT stresses are only small for the considered sizes $\Pi_7 = 0.159$ and $\Pi_7 = 0.2$. However, especially at $E = 60$ kPa, the CIN and CIT stresses cause a higher damage potential for the bigger particles.

For FIN and FIT stresses the damage potential varies with the Young's modulus E . However, there is no consistent trend. The damage potential due to CIN and CIT stresses, on the other hand, increases consistently with E and the impact is also pronounced.

In general, the biggest damage potentials result for $Re = 8$, $\alpha < 90^\circ$, $\Pi_7 = 0.2$, and $E = 60$ kPa, see Table 5.

The strong dependence on the Reynolds number Re is due to the fact that Re represents the ratio of inertial forces to viscous forces in a fluid. For fluid-induced stresses (FIN and FIT), the increased inertial forces at higher Reynolds numbers cause the fluid to exert more force on the surrounding surfaces. Also, the velocity gradients within the fluid become higher, resulting in higher shear stresses. In the context of contact-induced stresses (CIN and CIT), the increased inertial forces at higher Reynolds numbers result in more forceful solid-solid impacts, resulting in higher damage potential.

Compared to the impact of Re , the angle α has only a small impact, which is only noteworthy for smaller Re . However, in these cases, it is evident that a higher taper angle reduces the damage potential, because the more sudden the change in the diameter, the higher the chance for contacts and the bigger the changes in the velocity gradient.

The particle properties, Young's modulus and particle size, influence mainly the contact-induced stresses (CIN and CIT). This is because the contact forces directly depend on the Young's modulus and higher particle sizes of the as rigid considered particles make contacts more likely.

In summary, the above observations highlight that Re has the biggest impact on the damage potential. The influence of α is only measurable for $Re \leq 3$ and otherwise negligible. In the measurable cases, a larger taper angle leads to a generally smaller damage potential, for $\alpha \geq 45^\circ$. The strong change for $\alpha = 90^\circ$ is actually caused by the change of Re in the cross-section constriction. Furthermore, the damage potential due to contact depends strongly on the mechanical properties and size of the particle.

5.3 Validation

The underlying computational framework has already been rigorously validated [32, 33, 35, 37, 40, 41] and the velocity profiles obtained from PIV measurements on Herschel–Bulkley fluids could be reproduced by the simulations [44]. This section extends these validations by comparing the experimental results in Section 5.1 with the computational results in Section 5.2, focusing on the key observations that emerged from both approaches.

There is a strong correlation between the experimental and computational results. First, both methods revealed a significant dependence of the damage potential on the Reynolds number. As the Reynolds number increases, we consistently observed a corresponding increase in the damage potential in both experimental and numerical investigations. Second, our experimental and computational approaches agreed on the relatively small effect of geometry, specifically the taper angle, on the damage potential, as the damage potential due to the angle is much less pronounced compared to the dominant influence of the Reynolds number.

The agreement between experimental and numerical results in these key areas serves as a validation of our research methodology and results. This agreement not only reinforces the reliability of each approach, but also provides a more comprehensive and confident understanding of the phenomena under study. The consistency of the observations suggests that our numerical models accurately capture the essential physics of the system, lending credibility to both the experimental setup and the computational framework.

5.4 Discussion

Our findings, derived from both numerical and experimental studies, consistently point to the local Metzner–Reed Reynolds number as the most important parameter influencing the damage potential of particles during transport. This insight is critical because the Reynolds number is influenced by both process and design parameters, providing multiple avenues for reducing damage potential. In practice, there are several options, such as adjusting the flow rate or modifying the geometry to achieve optimal conditions.

Our research suggests that fluid deflection may not be a significant problem, primarily due to the nature of the fluid being considered, since the impact of the taper angle is less pronounced than that of the Reynolds number. However, our results indicate that it can still influence damage potential under certain conditions. This effect is particularly noticeable when the taper angle changes the local Reynolds number, highlighting the interrelated nature of these parameters. In addition, particle-specific factors such as Young’s modulus and size have been found to influence damage potential. However, it is important to note that these parameters are largely dependent on the type of fruit and its growing conditions, making them less controllable in practical applications.

The importance of the Metzner–Reed Reynolds number could also be applied to other critical components in transportation systems, such as valves and manifolds. Our results suggest that maintaining an approximately constant Reynolds number also in these parts could be an effective strategy for achieving uniform damage potential throughout the transport system. This approach could lead to more consistent design principles for different components of particle transport systems, particularly in industries that handle delicate materials such as fruit. This could lead to reduced waste, improved product quality, and potentially economic benefits in industries where minimizing particle damage is critical.

It is important to emphasize that while our results strongly suggest these conclusions, they require further validation across more possible scenarios and geometries. Applying our results to other geometries, such as aseptic valves, is a promising direction for future research, since these complex geometries could not be investigated in this study. Further studies are needed to validate the broader applicability of maintaining constant Reynolds numbers as a damage reduction strategy for various system components.

Besides investigating more system components, future research could also explore the applicability of these findings to a wider range of particle types and fluid properties. However, the experiments with two different fluids showed similar damage potential at comparable Reynolds numbers. In addition, long-term studies in real-world applications would be valuable to confirm the practical benefits of designing systems based on Reynolds number optimization.

In conclusion, our study provides a basis for understanding and potentially controlling particle damage in transport systems. By emphasizing the importance of the Reynolds number and providing insights into the role of geometry and particle properties, the results highlight potential optimizations in system design. In addition, these results emphasize the need for further, more in-depth studies considering a wider range of materials and system components to determine further potential improvements in real-world systems.

6 Summary and conclusions

This study investigates the potential for damage of fruits immersed in a Herschel–Bulkley fluid during transport through cross-section constrictions, using both experiments and simulations. Industrial peach preparations are therefore conveyed in three different pipe geometries at a technical scale. Two different volume flow rates are applied, and the disintegration of the fruit pieces is quantified by wet sieving. Four-way coupled fully resolved particulate flow simulations are realized using HLBM. Its goal is the quantification of the damage potential and also the identification of parameters with a strong correlation.

The results reveal that the local Reynolds number has the most significant impact on the damage potential. The taper angle, a geometric parameter, has a limited effect, but it can influence the damage potential, especially if it influences the local Reynolds number. The particle parameters, including Young’s modulus and size, also contribute to the damage potential, but they are largely dependent on the type of fruit and its growing conditions.

The findings therefore suggest that the damage potential is reducible by adjusting the process conditions or by modifying the geometry to control the local Reynolds number. This, in turn, results in end products of higher quality and value.

Acknowledgements: This IGF Project of the FEI is/was supported within the programme for promoting the Industrial Collective Research (IGF) of the Federal Ministry of Economic Affairs and Climate Action (BMWK), based on a resolution of the German Parliament. Project 21096 N. This work was performed on the HoreKa supercomputer funded by the Ministry of Science, Research and the Arts Baden-Württemberg and by the Federal Ministry of Education and Research. The authors acknowledge support by the state of Baden-Württemberg through bwHPC. The authors of the

Technical University of Berlin would like to thank for the funding of Deutsche Forschungsgemeinschaft (DFG) for the multiscale Particle-Image-Velocimetry (PIV)-system in the frame of project 43172972.

Author contribution statement: **J. E. Marquardt:** Conceptualization, Methodology, Software, Validation, Formal analysis, Investigation, Data curation, Writing - Original Draft, Writing - Review & Editing, Visualization, Project administration, Funding acquisition; **B. Eysel:** Conceptualization, Methodology, Validation, Formal analysis, Investigation, Data curation, Writing - Original Draft, Writing - Review & Editing, Visualization, Project administration. **M. Sadric:** Software, Formal analysis, Data curation, Writing - Review & Editing. **C. Rauh:** Resources, Supervision, Project administration, Funding acquisition. **M. J. Krause:** Software, Resources, Supervision, Project administration, Funding acquisition.

References

- [1] Mostafa Barigou, PG Fairhurst, PJ Fryer, and J-P Pain. Concentric flow regime of solid–liquid food suspensions: theory and experiment. *Chemical engineering science*, 58(9):1671–1686, 2003. doi:10.1016/S0009-2509(03)00003-4.
- [2] Alexandra Legrand, Marc Berthou, and Luc Fillaudeau. Characterization of solid–liquid suspensions (real, large non-spherical particles in non-newtonian carrier fluid) flowing in horizontal and vertical pipes. *Journal of food engineering*, 78(1):345–355, 2007. doi:10.1016/j.jfoodeng.2005.10.002.
- [3] C Lareo, PJ Fryer, and M Barigou. The fluid mechanics of two-phase solid-liquid food flows: a review. *Food and Bioproducts Processing*, 75(2):73–105, 1997. doi:10.1205/096030897531405.
- [4] Efstathios Michaelides, Clayton T Crowe, and John D Schwarzkopf, editors. *Multiphase flow handbook*. CRC Press, 2 edition, 2016.
- [5] Christopher E Brennen. *Fundamentals of Multiphase Flow*. Cambridge University Press, 2005.
- [6] Zhiguo Li, Fengli Miao, and James Andrews. Mechanical models of compression and impact on fresh fruits. *Comprehensive Reviews in Food Science and Food Safety*, 16(6):1296–1312, 2017. doi:10.1111/1541-4337.12296.
- [7] MS Pervez and TH Solomon. Long-term tracking of neutrally buoyant tracer particles in two-dimensional fluid flows. *Experiments in fluids*, 17(3):135–140, 1994. doi:10.1007/BF00190909.
- [8] Choeng Ryul Choi and Chang Nyung Kim. Inertial migration and multiple equilibrium positions of a neutrally buoyant spherical particle in poiseuille flow. *Korean Journal of Chemical Engineering*, 27:1076–1086, 2010. doi:10.1007/s11814-010-0214-7.
- [9] Varghese Mathai, Matthijs WM Neut, Erwin P van der Poel, and Chao Sun. Translational and rotational dynamics of a large buoyant sphere in turbulence. *Experiments in fluids*, 57:1–10, 2016. doi:10.1007/s00348-016-2136-6.
- [10] BAJC Chun and AJC Ladd. Inertial migration of neutrally buoyant particles in a square duct: An investigation of multiple equilibrium positions. *Physics of Fluids*, 18(3), 2006. doi:10.1063/1.2176587.
- [11] Vincent Loisel, Micheline Abbas, Olivier Masbernat, and Eric Climent. The effect of neutrally buoyant finite-size particles on channel flows in the laminar-turbulent transition regime. *Physics of Fluids*, 25(12), 2013. doi:10.1063/1.4848856.
- [12] Teng-hu Wu, Xue-ming Shao, and Zhao-sheng Yu. Fully resolved numerical simulation of turbulent pipe flows laden with large neutrally-buoyant particles. *Journal of Hydrodynamics, Ser. B*, 23(1):21–25, 2011. doi:10.1016/S1001-6058(10)60083-2.
- [13] Mehdi Niazi Ardekani, Léa Al Asmar, Francesco Picano, and Luca Brandt. Numerical study of heat transfer in laminar and turbulent pipe flow with finite-size spherical particles. *International Journal of Heat and Fluid Flow*, 71:189–199, 2018. doi:10.1016/j.ijheatfluidflow.2018.04.002.
- [14] M Eesa and MJCES Barigou. Cfd investigation of the pipe transport of coarse solids in laminar power law fluids. *Chemical Engineering Science*, 64(2):322–333, 2009. doi:10.1016/j.ces.2008.10.004.
- [15] Zhiguo Li and Colin Thomas. Quantitative evaluation of mechanical damage to fresh fruits. *Trends in Food Science & Technology*, 35(2):138–150, February 2014. doi:10.1016/j.tifs.2013.12.001.
- [16] Christian Schmitt. *Experimentelle Vergleichsstudien zur Förderung von Lebensmittelsuspensionen mittels Pumpen anhand unterschiedlicher lebensmittelbasierter Modellsysteme*. PhD thesis, Kassel, Universität Kassel, Fachbereich Ökologische Agrarwissenschaften, Fachgebiet Agrartechnik, 06 2018.

- [17] Stefan Wollny and Reinhard Sperling. Partikelbeanspruchung in gerührten behältern. *Chemie Ingenieur Technik*, 79(3):199–208, 2007. doi:10.1002/cite.200600129.
- [18] Martin Wille, Gert Langer, and Udo Werner. Pda measurement of drop size distribution for liquid-liquid dispersing in agitated tanks. *Chemical Engineering & Technology: Industrial Chemistry-Plant Equipment-Process Engineering-Biotechnology*, 24(5):475–479, 2001. doi:10.1002/1521-4125(200105)24:5<475::AID-CEAT475>3.0.CO;2-L.
- [19] K. C. Sahu, P. Valluri, P. D. M. Spelt, and O. K. Matar. Linear instability of pressure-driven channel flow of a newtonian and a herschel-bulkley fluid. *Physics of Fluids*, 19(12):122101, 2007. doi:10.1063/1.2814385.
- [20] Fridtjov Irgens. *Rheology and Non-Newtonian Fluids*. Springer International Publishing, Cham, 2014. doi:10.1007/978-3-319-01053-3.
- [21] Benjamin Nassauer and Meinhard Kuna. Contact forces of polyhedral particles in discrete element method. *Granular Matter*, 15(3):349–355, 2013. doi:10.1007/s10035-013-0417-9.
- [22] André S. Carvalho and Jorge M. Martins. Exact restitution and generalizations for the hunt–crossley contact model. *Mechanism and Machine Theory*, 139:174–194, 2019. doi:10.1016/j.mechmachtheory.2019.03.028.
- [23] Adrian Kummerländer, Tim Bingert, Fedor Bukreev, Luiz Eduardo Czelusniak, Davide Dapelo, Nicolas Hafen, Marc Heinzelmann, Shota Ito, Julius Jeßberger, Halim Kusumaatmaja, Jan E. Marquardt, Michael Rennick, Tim Pertz, František Prinz, Martin Sadric, Maximilian Schecher, Stephan Simonis, Pascal Sitter, Dennis Teutscher, Mingliang Zhong, and Mathias J. Krause. OpenLB Release 1.7: Open Source Lattice Boltzmann Code, 2024. doi:10.5281/zenodo.10684609.
- [24] Mathias J. Krause, Adrian Kummerländer, Samuel J. Avis, Halim Kusumaatmaja, Davide Dapelo, Fabian Klemens, Maximilian Gaedtke, Nicolas Hafen, Albert Mink, Robin Trunk, Jan E. Marquardt, Marie-Luise Maier, Marc Haussmann, and Stephan Simonis. OpenLB—Open source lattice Boltzmann code. *Computers & Mathematics with Applications*, 81:258–288, 2021. doi:10.1016/j.camwa.2020.04.033.
- [25] Sauro Succi. *The lattice Boltzmann equation: for fluid dynamics and beyond*. Oxford university press, 2001.
- [26] Timm Krüger, Halim Kusumaatmaja, Alexandr Kuzmin, Orest Shardt, Goncalo Silva, and Erlend Magnus Vigen. *The Lattice Boltzmann Method*. Graduate Texts in Physics. Springer, 2017. doi:10.1007/978-3-319-44649-3.
- [27] Michael C. Sukop and Daniel T. Thorne. *Lattice Boltzmann Modeling: An introduction for geoscientists and Engineers*. Springer, 2., corrected print edition, 2006. doi:10.1007/978-3-540-27982-2.
- [28] P. L. Bhatnagar, E. P. Gross, and M. Krook. A model for collision processes in gases. i. small amplitude processes in charged and neutral one-component systems. *Physical Review*, 94(3):511–525, 1954. doi:10.1103/PhysRev.94.511.
- [29] Y. H Qian, D D’Humières, and P Lallemand. Lattice BGK models for navier-stokes equation. *Europhysics Letters (EPL)*, 17(6):479–484, February 1992. doi:10.1209/0295-5075/17/6/001.
- [30] Susana Gabbanelli, German Drazer, and Joel Koplik. Lattice boltzmann method for non-newtonian (power-law) fluids. *Physical Review E*, 72(4):046312, 2005. doi:10.1103/PhysRevE.72.046312.
- [31] Davide Dapelo, Robin Trunk, Mathias J. Krause, and John Bridgeman. Towards lattice-boltzmann modelling of unconfined gas mixing in anaerobic digestion. *Computers & Fluids*, 180:11–21, 2019. doi:10.1016/j.compfluid.2018.12.008.
- [32] Mathias J. Krause, Fabian Klemens, Thomas Henn, Robin Trunk, and Hermann Nirschl. Particle flow simulations with homogenised lattice boltzmann methods. *Particuology*, 34:1–13, Oct 2017. doi:10.1016/j.partic.2016.11.001.
- [33] Robin Trunk, Jan Marquardt, Gudrun Thäter, Hermann Nirschl, and Mathias J. Krause. Towards the simulation of arbitrarily shaped 3d particles using a homogenised lattice boltzmann method. *Computers & Fluids*, 172:621–631, Aug 2018. doi:10.1016/j.compfluid.2018.02.027.
- [34] Marc Haussmann, Nicolas Hafen, Florian Raichle, Robin Trunk, Hermann Nirschl, and Mathias J. Krause. Galilean invariance study on different lattice boltzmann fluid–solid interface approaches for vortex-induced vibrations. *Computers & Mathematics with Applications*, 80:671–691, Sep 2020. doi:10.1016/j.camwa.2020.04.022.
- [35] Robin Trunk, Timo Weckerle, Nicolas Hafen, Gudrun Thäter, Hermann Nirschl, and Mathias J. Krause. Revisiting the homogenized lattice boltzmann method with applications on particulate flows. *Computation*, 9(22):11, Feb 2021. doi:10.3390/computation9020011.
- [36] Nicolas Hafen, Julia R.D. Thieringer, Jörg Meyer, Mathias J. Krause, and Achim Dittler. Numerical investigation of detachment and transport of particulate structures in wall-flow filters using lattice Boltzmann methods. *J. Fluid Mech.*, 956:A30, February 2023. doi:10.1017/jfm.2023.35.

- [37] Jan E. Marquardt, Nicolas Hafen, and Mathias J. Krause. A novel particle decomposition scheme to improve parallel performance of fully resolved particulate flow simulations. *Journal of Computational Science*, 78:102263, 2024. doi:10.1016/j.jocs.2024.102263.
- [38] A. Kupershtokh, D. Medvedev, and D. Karpov. On equations of state in a lattice Boltzmann method. *Computers & Mathematics with Applications*, 58:965–974, 2009. doi:10.1016/j.camwa.2009.02.024.
- [39] Binghai Wen, Chaoying Zhang, Yusong Tu, Chunlei Wang, and Haiping Fang. Galilean invariant fluid–solid interfacial dynamics in lattice Boltzmann simulations. *Journal of Computational Physics*, 266:161–170, 2014. doi:10.1016/j.jcp.2014.02.018.
- [40] Jan E. Marquardt, Ulrich J. Römer, Hermann Nirschl, and Mathias J. Krause. A discrete contact model for complex arbitrary-shaped convex geometries. *Particuology*, 80:180–191, 2023. doi:10.1016/j.partic.2022.12.005.
- [41] Jan E. Marquardt, Nicolas Hafen, and Mathias J. Krause. A novel model for direct numerical simulation of suspension dynamics with arbitrarily shaped convex particles. *Computer Physics Communications*, 304:109321, 2024. doi:10.1016/j.cpc.2024.109321.
- [42] A. B. Metzner and J. C. Reed. Flow of non-newtonian fluids—correlation of the laminar, transition, and turbulent-flow regions. *AIChE J.*, 1(4):434–440, 1955. doi:10.1002/aic.690010409.
- [43] B. Eysel, S Schurr, Q. Phan, C. McHardy, and C. Rauh. Herstellung von brechungsindexangepassten zwei-phasenmodellstoffsystemen zur imitation von fruchtzubereitungen für optische strömungsmessungen. *Proceedings der 28. GALA-Fachtagung "Experimentelle Strömungsmechanik"*, 28:48.1–48.8, 2021.
- [44] B. Eysel, J. E. Marquardt, M.J. Krause, C. McHardy, and C. Rauh. Charakterisierung der rohrströmung komplexer fest-flüssigmodellstoffsysteme mittels stereo piv. *Proceedings der 30. GALA-Fachtagung "Experimentelle Strömungsmechanik"*, 30:32–1–32–8, 2023.
- [45] E.E. Finney. Dynamic elastic properties of some fruits during growth and development. *Journal of Agricultural Engineering Research*, 12(4):249–256, 1967. doi:10.1016/s0021-8634(67)80043-x.
- [46] Zhong Chen, Umesh Gandhi, Jinwoo Lee, and R.H. Wagoner. Variation and consistency of young’s modulus in steel. *Journal of Materials Processing Technology*, 227:227–243, 2016. doi:10.1016/j.jmatprotec.2015.08.024.
- [47] Gökçen Yıldız, Nazmi İzli, Halil Ünal, and Vildan Uylaşer. Physical and chemical characteristics of goldenberry fruit (*Physalis peruviana* L.). *Journal of Food Science and Technology*, 52(4):2320–2327, 2014. doi:10.1007/s13197-014-1280-3.
- [48] Jonas Latt, Bastien Chopard, Orestis Malaspinas, Michel Deville, and Andreas Michler. Straight velocity boundaries in the lattice Boltzmann method. *Phys. Rev. E*, 77(5):056703, May 2008. Publisher: American Physical Society. doi:10.1103/PhysRevE.77.056703.
- [49] M’hamed Bouzidi, Mouaouia Firdaouss, and Pierre Lallemand. Momentum transfer of a Boltzmann-lattice fluid with boundaries. *Physics of Fluids*, 13(11):3452–3459, 2001. doi:10.1063/1.1399290.